European Radiology (2023) 33:7686–7696
https://doi.org/10.1007/s00330-023-09742-6

European Radiology
EUROPEAN SOCIETY OF RADIOLOGY

MAGNETIC RESONANCE

AI-assisted compressed sensing and parallel imaging sequences for MRI of patients with nasopharyngeal carcinoma: comparison of their capabilities in terms of examination time and image quality

Haibin Liu[1] · Dele Deng[1] · Weilong Zeng[1] · Yingyi Huang[1] · Chunling Zheng[1] · Xinyang Li[2] · Hui Li[1] · Chuanmiao Xie[1] · Haoqiang He[1] · Guixiao Xu[1]

Received: 23 September 2022 / Revised: 21 March 2023 / Accepted: 14 April 2023 / Published online: 23 May 2023

Abstract

Objective To compare examination time and image quality between artificial intelligence (AI)–assisted compressed sensing (ACS) technique and parallel imaging (PI) technique in MRI of patients with nasopharyngeal carcinoma (NPC).

Methods Sixty-six patients with pathologically confirmed NPC underwent nasopharynx and neck examination using a 3.0-T MRI system. Transverse T2-weighted fast spin-echo (FSE) sequence, transverse T1-weighted FSE sequence, post-contrast transverse T1-weighted FSE sequence, and post-contrast coronal T1-weighted FSE were obtained by both ACS and PI techniques, respectively. The signal-to-noise ratio (SNR), contrast-to-noise ratio (CNR), and duration of scanning of both sets of images analyzed by ACS and PI techniques were compared. The images from the ACS and PI techniques were scored for lesion detection, margin sharpness of lesions, artifacts, and overall image quality using the 5-point Likert scale.

Results The examination time with ACS technique was significantly shorter than that with PI technique ($p < 0.0001$). The comparison of SNR and CNR showed that ACS technique was significantly superior with PI technique ($p < 0.005$). Qualitative image analysis showed that the scores of lesion detection, margin sharpness of lesions, artifacts, and overall image quality were higher in the ACS sequences than those in the PI sequences ($p < 0.0001$). Inter-observer agreement was evaluated for all qualitative indicators for each method, in which the results showed satisfactory-to-excellent agreement ($p < 0.0001$).

Conclusion Compared with the PI technique, the ACS technique for MR examination of NPC can not only shorten scanning time but also improve image quality.

Clinical relevance statement The artificial intelligence (AI)–assisted compressed sensing (ACS) technique shortens examination time for patients with nasopharyngeal carcinoma, while improving the image quality and examination success rate, which will benefit more patients.

Key Points

- *Compared with the parallel imaging (PI) technique, the artificial intelligence (AI)–assisted compressed sensing (ACS) technique not only reduced examination time, but also improved image quality.*
- *Artificial intelligence (AI)–assisted compressed sensing (ACS) pulls the state-of-the-art deep learning technique into the reconstruction procedure and helps find an optimal balance of imaging speed and image quality.*

Keywords Compressed sensing · Parallel imaging · Magnetic resonance imaging · Nasopharyngeal carcinoma

Haibin Liu and Dele Deng contributed equally.

✉ Haoqiang He
hehq@sysucc.org.cn

✉ Guixiao Xu
xugx@sysucc.org.cn

[1] Department of Radiology, State Key Laboratory of Oncology in South China, Guangdong Key Laboratory of Nasopharyngeal Carcinoma Diagnosis and Therapy, Sun Yat-sen University Cancer Center, Guangzhou 510060, People's Republic of China

[2] United Imaging Healthcare, Shanghai, People's Republic of China

Abbreviations

ACS	Artificial intelligence (AI)–assisted compressed sensing
AI	Artificial intelligence
AiCE	Advanced intelligent Clear IQ Engine
CNN	Convolutional neural network
CNR	Contrast-to-noise ratio
CS	Compression sensing
CT	Computed tomography
DLR	Deep learning reconstruction
FOV	Field-of-view
FSE	Fast spin-echo
HF	Half-Fourier
MRI	Magnetic resonance imaging
NKUC	Nonkeratinizing undifferentiated carcinoma
NPC	Nasopharyngeal carcinoma
PACS	Picture Archiving and Communication System
PI	Parallel imaging
ResNet	Residual Neural Network
ROI	Region of interest
SD	Standard deviation
SI	Signal intensity
SNR	Signal-to-noise ration

Introduction

Nasopharyngeal carcinoma (NPC) is an endemic disease in Southeast Asia, especially in some southern provinces of mainland China [1]. Magnetic resonance imaging (MRI) is widely used in the diagnosis, staging, and efficacy evaluation of NPC. Compared with computed tomography (CT), MRI can better identify early-stage NPC (stages I–II) and has superior sensitivity and specificity for discriminating adjacent soft tissue invasion, skull base invasion, cranial nerve invasion, and retropharyngeal lymph node involvement [2–4].

Although the advantages of MRI are noticeable, the time-consuming feature of MRI can lead to patients' fatigue and motion artifacts, reducing the quality of images. K-space under-sampling is currently the main method for reducing MRI scan time [5]. There are three main approaches to perform k-space under-sampling, including Half Fourier (HF) imaging, parallel imaging (PI), and compression sensing (CS) [6]. The HF technique is based on the Hermitian conjugate symmetry of the k-space. Only half of the k-space data are acquired in the phase encoding direction under ideal conditions, and the other half can be calculated and filled according to the conjugate symmetry of the k-space [7–9]. The deficiency of HF is that Gibbs artifacts are generated and signal-to-noise ratio (SNR) of an image decreases inevitably. The PI technique relies on the use of a receiver coil array to collect under-sampled k-space data and on specialized algorithms to reconstruct the complete field-of-view (FOV) images [10, 11]. PI is a commonly used acceleration tool in clinical applications, while image quality at high-acceleration factors may be reduced by noise amplification and under-sampled artifacts. The CS technique provides a new approach to recover imaging data from under-sampled k-space through the exploitation of sparsity. A small number of signals acquired by incoherence sampling are reconstructed with a high-probability using a reconstruction algorithm, and finally higher quality MR images are obtained by the Fourier transform [12–14].

In recent years, CS has been widely used as a new under-sampled k-space method. However, its insufficient sparsity may lead to noise-like aliasing artifacts when excessive acceleration factors are employed. Therefore, some MR vendors have introduced deep learning reconstruction (DLR) to improve image quality [15–17], such as the Advanced intelligent Clear IQ Engine (AiCE) developed by Canon Medical Systems Corporation [18]. A new acceleration method, namely artificial intelligence (AI)–assisted compressed sensing (ACS), was developed by United Imaging Intelligence (UII) and United Imaging Healthcare (UIH), incorporating CS, HF, and PI to innovatively introduce deep learning neural networks as AI modules into the reconstruction process [19].

MRI is the most appropriate method for localization and qualitative and staging diagnosis of NPC [20–23]. T2-weighted fast spin-echo (FSE), T1-weighted FSE, and contrast-enhanced T1-weighted FSE are key sequences in MRI of NPC [24]. Conventional MRI scans of NPC are dominated by FSE sequences with PI [25], and in some sequences, a combination of fat suppression is required to determine whether the tumor has bone marrow infiltration of the skull base [26, 27]. In addition, the MRI of NPC must be scanned in combination with the nasopharynx and neck to facilitate clinical staging. The longer total time of MRI scans due to the combined nasopharyngeal and neck scan and the adoption of FSE sequences with a longer time, resulting in failure of some patients in completion of the examination because of intolerance. The present study aimed to apply the innovative ACS technique to FSE sequences to explore the capabilities of ACS in improving the time and quality of MRI of NPC.

Methods

Study population

The study was approved by the institutional review board of our hospital (Approval No. B2020-417). From August 2021 to December 2021, a total of 72 patients with confirmed or suspected NPC underwent nasopharynx and neck examination using a 3.0-T MR system. The inclusion criteria were as follows: (1) newly diagnosed, untreated patients with

Table 1 Patients' characteristics

Characteristics	Values
Number of patients (%)	66
Mean age ± SD (range); years	44 ± 11 (18–64)
Gender	
Male	44 (66.7%)
Female	22 (33.3%)
Histological type	
NKUC	66 (100%)
T stage	
T1	7 (10.6%)
T2	6 (9.1%)
T3	42 (63.6%)
T4	11 (16.7%)
N stage	
N0	1 (1.5%)
N1	30 (45.5%)
N2	18 (27.2%)
N3	17 (25.8%)
M stage	
M0	61 (92.4%)
M1	5 (7.6%)
AJCC stage	
I	2 (3%)
II	8 (12.1%)
III	30 (45.5%)
IV	26 (39.4%)

Abbreviations: *SD*, standard deviation; *NKUC*, nonkeratinizing undifferentiated carcinoma

NPC; (2) patients who aged ≥ 18 years old. The exclusion criteria were as follows: (1) no pathological confirmation of NPC; (2) poor patient compliance, incomplete data, or severe motion artifacts. Finally, 66 patients who were pathologically diagnosed with NPC were included in this study. Patients' characteristics are presented in Table 1.

MRI acquisition

All MRI measurements were performed on a 3.0-T MR machine (uMR790; United Imaging Healthcare Co., Ltd) with a head and neck combined coil. Transverse T2-weighted FSE sequences and transversal, sagittal, and coronal plane T1-weighted FSE images were obtained before contrast injection. After the injection of gadopentetate dimeglumine at a dose of 0.1 mmol/kg, T1-weighted transverse, sagittal, and coronal sequences (with fat saturation) were obtained using parameters similar to pre-injection imaging.

Transverse T2-weighted FSE sequence, transverse T1-weighted FSE sequence, post-contrast transverse T1-weighted FSE sequence, and post-contrast coronal T1-weighted FSE with fat suppression were experimental sequences, which were obtained by both ACS and PI techniques, respectively. The periods of examinations were recorded for all patients. The parameters (TR, TE, ETL, etc.) used in the ACS sequences and PI sequences of the same patient are consistent; details of parameters of ACS and PI sequences are listed in Table 2.

ACS

ACS incorporates CS, PI, HF, and AI to provide an improved MR acceleration solution. It innovatively introduces AI module based on deep neural networks. The goal of the AI module in ACS is to learn the features of fully sampled high-quality images without reconstruction artifacts, converting the obtained full k-space data into the image space, as the target output. The AI module is trained based on the designed Residual Neural Network (ResNet), which is widely used in the convolutional neural network (CNN) [17, 28–30]. The structure of the network consists of two convolutional operations and a skip connection. A long skip-over connection between the input and output of the network is added to learn the residual between the fully sampled and under-sampled images to improve the convergence rate during learning. To further improve the quality of the reconstructed images, a least-squares generative adversarial network training strategy is used [31]. The network design is shown in Fig. 1. The under-sampled images provide the information really obtained during the scanning process. The prior knowledge of the input data is maintained by the important Data Consistency Checking model in the internal network, while the parameters in the Feature Detection and Image Optimization processes will be optimized during the training phase until the prediction of the network reaches the optimal state. During the training phase of the AI model, a great number of full k-space data were collected and retrospectively under-sampled and converted to the image space as input. "This FDA-approved deep learning assisted reconstruction method was trained based on two million fully sampled slices previously acquired with phantom (2%) and volunteers (98%)" [31].

The compressed AI module is integrated into the iterative reconstruction program of the compressed sensing framework to get the final images. ACS follows the principle of compressed sensing and uses the learning ability of AI module at the same time. This effective combination fulfills the advantages of deep learning and also enables the AI module is controllable.

Quantitative image analysis

The quantitative image analysis was performed on a workstation (uWS-MrR005; United Imaging Healthcare

Table 2 MRI sequences and parameters

Sequence parameter	Tra T2WI FSE ACS	Tra T2WI FSE PI	Tra T1WI FSE ACS	Tra T1WI FSE PI	Post-contrast Tra T1WI FSE ACS	Post-contrast Tra T1WI FSE PI	Post-contrast Cor T1WI FSE ACS	Post-contras Cor T1WI FSE PI
Fov (mm)	240×240	240×240	240×240	240×240	240×240	240×240	280×240	280×240
TR/TE (ms)	4800/120	4800/120	662/8.16	662/8.16	789/8.12	789/8.12	576/10.82	576/10.82
Matrix	384×269	384×269	384×307	384×307	384×307	384×307	352×226	352×226
ETL	28	28	2	2	2	2	4	4
Bandwidth (Hz)	260	260	280	280	250	250	250	250
Average	1	1	1	1	1	1	1.2	1.2
Number slices	40	40	40	40	40	40	24	24
Spatial resolution	0.89 × 0.63 × 5	0.89 × 0.63 × 5	0.78 × 0.63 × 5	0.78 × 0.63 × 5	0.78 × 0.63 × 5	0.78 × 0.63 × 5	1.06 × 0.8 × 2	1.06 × 0.8 × 2
Acquisition	ACS	PI	ACS	PI	ACS	PI	ACS	PI
Accelerating factors	2.25	2	2.25	2	2.25	2	2.5	2
Fat suppression	No	No	No	No	No	No	Yes	Yes

ACS, AI-assisted compressed sensing; *PI*, parallel imaging; *Tra T2WI*, transverse T2-weighted image; *Tra T1WI*, transverse T1-weighted image; *Cor T1WI*, coronal T1-weighted image

Co., Ltd.). The images generated by both ACS and PI techniques were required to measure the signal intensity (SI) and the standard deviation (SD) by placing in regions of interest (ROIs). ROIs were placed on two sets of images of transverse T2-weighted FSE sequence, transverse T1-weighted FSE sequence, post-contrast transverse T1-weighted FSE sequence, and post-contrast coronal T1-weighted FSE with fat suppression sequence. Then, the following data were measured at the largest lesion in both sets of images: The SI of the lesion, the SI of the lateral pterygoid muscle (ROI should be placed on the image of the contralateral lateral pterygoid muscle if the ipsilateral lateral pterygoid muscle has been invaded), the SD at the four corners (the top-left, top-right, bottom-left, and bottom-right corners) of background in the same layer image. The SNR and the CNR were calculated using the following formula [32]:

$$\mathrm{SNR} = \frac{0.66 \times S}{SD} \times \sqrt{\frac{10}{d}} \quad (1)$$

where S is the SI lesion, SD is the mean standard deviation of the SI at the four corners of background noise, and d is the slice thickness.

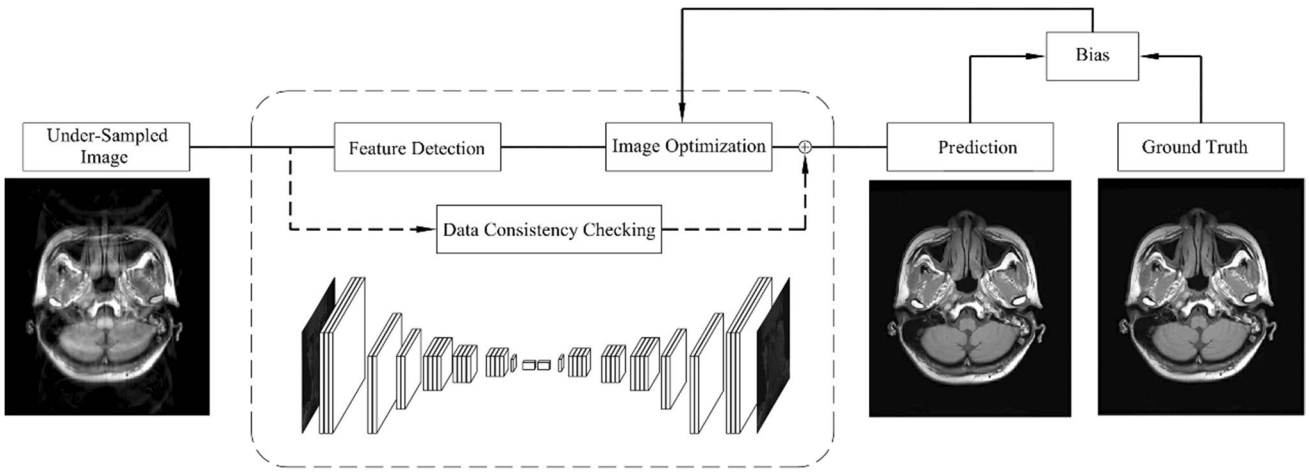

Fig. 1 The AI module in ACS mitigates reconstruction artifacts at high acceleration levels

To calculate the CNR, the following formula was applied:

$$\mathrm{CNR} = \frac{SI_{\mathrm{tissue1}} - SI_{\mathrm{tissue2}}}{SD} \quad (2)$$

where SI_{tissue1} and SI_{tissue2} are the SI of the lesion and the lateral pterygoid muscle, respectively; *SD* is the mean standard deviation of the signal intensity at the four corners of background noise.

MRI of the neck is particularly important in the evaluation of lymph node metastasis in NPC. The evaluation of the SI in the lower neck region was performed by measuring the SNR of the trapezius muscle. ROIs were placed on the two image sets (ACS and PI) of the trapezius muscle from the post-contrast coronal T1-weighted FSE with fat suppression sequence to obtain the SI of the trapezius muscle. When the SD at the four corner signals of background noise was measured, the mean and the SD were calculated. The SNR of the trapezius muscle was calculated using Eq. (1).

Qualitative image analysis

The qualitative image analysis was carried out using the Picture Archiving and Communication System (PACS) (Centricity™ PACS; GE Medical Systems). All the imaging analyses were performed by two radiologists (H.L. and C.M.X.) who had 18 and 34 years of experience in the diagnosis of NPC. Two readers were individually blinded to patients' clinical data and evaluated lesion detection, margin sharpness of lesions, artifacts, and overall image quality using a 5-point scoring system. In the present study, the lesion detection was scored as follows: 1, poor, almost invisible; 2, fair, lesions were partially visible; 3, moderate, lesions could be detected, while they were unclear; 4, good, lesions could be detected, and anatomical details were relatively clear; 5, excellent, lesions were easily detected, and anatomical details were very clear. The margin sharpness of lesions was rated as follows: 1, unreadable; 2, extremely blur; 3, moderately blur; 4, mildly blur; 5, no blur. The artifacts were scored as follows: 1, unreadable; 2, severe artifact; 3, moderate artifact; 4, mild artifact; 5, no artifact. The overall image quality was scored as follows: 1, poor; 2, fair; 3, moderate; 4, good; 5, excellent.

Statistical analysis

The statistical analysis was carried out using SPSS 26.0 software (IBM). The examination time and the values of the SNR and CNR were compared between ACS and PI sequences. All measurement data were expressed as the mean ± SD. Normality of data was tested by the Kolmogorov-Smirnov test. The paired sample *t*-test was used for the analysis of normally distributed data, and the Wilcoxon signed-rank test was utilized for the analysis of abnormally distributed data. The image quality scores of sequences with ACS and PI techniques were also tested using the Wilcoxon signed-rank test. Weighted kappa statistic and $\chi 2$ test were used to evaluate the inter-observer agreement of imaging analyses for each qualitative indicator. The kappa coefficients for inter-observer agreements were interpreted as follows: <0.20, very weak; 0.21–0.40, weak; 0.41–0.60, moderate; 0.61–0.80, satisfactory; and 0.81–1.00, excellent. $p<0.05$ was considered statistically significant.

Results

Two representative cases are illustrated in Figs. 2 and 3.

The comparison of examination time (Fig. 4) showed that the time of FSE sequences with ACS was significantly shorter than that of FSE sequences with PI, and the overall examination time of the ACS sequences and the PI sequences showed a statistical difference. The comparison of examination time showed that the time of T2-weighted sequences in the transverse planes with ACS was significantly shorter than that with PI (ACS (40.08 ± 1.33 s) vs. PI (60.21 ± 3.24 s), $p<0.0001$). The time of T1-weighted sequences in the transverse planes with ACS was significantly shorter than that with PI (ACS (74.91 ± 2.76 s) vs. PI (107.54 ± 5.89 s), $p<0.0001$). The time of post-contrast T1-weighted sequences in the transverse planes with ACS was significantly shorter than that with PI (ACS (92.40 ± 2.82 s) vs. PI (129.72 ± 5.66 s), $p<0.0001$). The time of post-contrast T1-weighted sequences in the coronal planes with ACS was significantly shorter than that with PI (ACS (127.78 ± 9.74 s) vs. PI (218.21 ± 16.13 s), $p<0.0001$). The total time of 4 sequences using ACS and PI was 335.17 ± 11.40 and 515.67 ± 21.80 s, respectively ($p<0.0001$).

The comparison of SNR (Table 3 and Fig. 5) showed that the SNR values of FSE sequences with ACS were significantly higher than those of FSE sequences with PI. The SNR values of T2-weighted sequences in the transverse planes with ACS were significantly higher than those with PI (ACS (182.07 ± 41.69) vs. PI (145.27 ± 38.05), $p<0.0001$). The SNR values of T1-weighted sequences in the transverse planes with ACS were significantly higher than those with PI (ACS (183.53 ± 31.36) vs. PI (147.02 ± 27.11), $p<0.0001$). The SNR values of post-contrast T1-weighted sequences in the transverse planes with ACS were significantly higher than those with PI (ACS (312.43 ± 56.59) vs. PI (245.89 ± 46.68), $p<0.0001$). The SNR values of post-contrast T1-weighted sequences in the coronal planes with ACS were significantly higher than those with PI (ACS

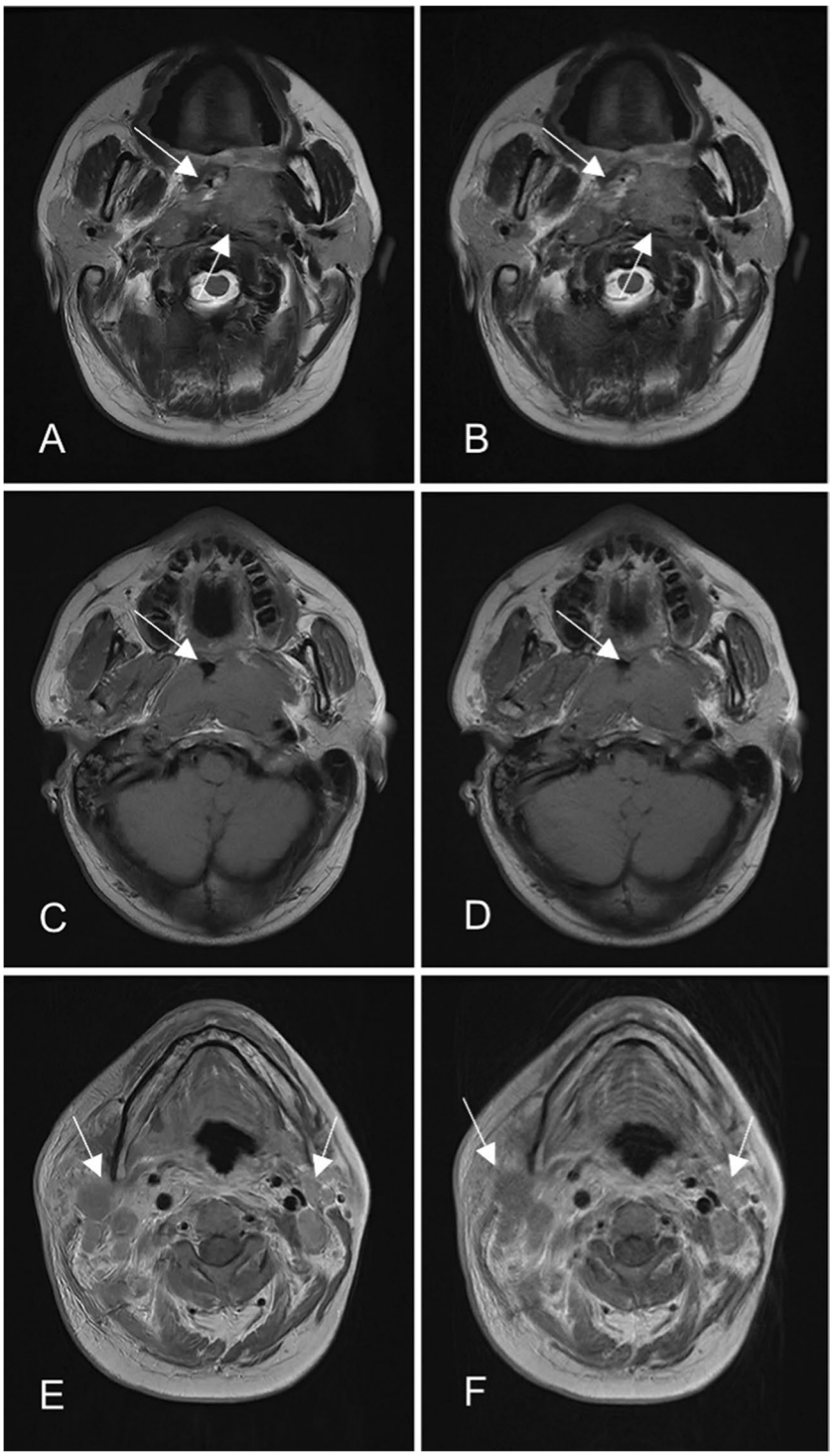

Fig. 2 A 34-year-old male patient with NPC. The MRI sequences and examination time were summarized as follows: T2-weighted FSE sequences in the transverse planes: (**A**) with ACS technique (39.6 s); (**B**) with PI technique (59.0 s); T1-weighted FSE sequences in the transverse planes: (**C**) with ACS technique (74.8 s); (**D**) with PI technique (105.4 s); post-contrast T1-weighted FSE sequences in the transverse plane: (**E**) with ACS technique (92.1 s); (**F**) with PI technique (129.9 s). The border of NPC was clearer for FSE sequences with ACS (**A**, **C** arrows) than for FSE sequences with PI (**B**, **D** arrows); the scan time was shorter with ACS (**E**) than with PI (**F**), and the artifacts of swallowing motion could be effectively suppressed (**E**, **F** arrows) due to shortening of time

(189.05 ± 60.84) vs. PI (140.82 ± 43.26), $p < 0.0001$). The SNR values of the trapezius were also statistically significant in post-contrast coronal T1-weighted FSE with fat suppression sequences (ACS (94.76 ± 27.08) vs. PI (78.63 ± 23.00), $p < 0.0001$). As for CNR values, the FSE sequences with ACS were also significantly higher than those of FSE sequences with PI (Table 3 and Fig. 6). The CNR values of T2-weighted sequences in the transverse planes with ACS were significantly higher than those sequences with PI (ACS (6.21 ± 3.00) vs. PI (5.52 ± 3.05), $p < 0.0027$). The CNR values of T1-weighted sequences in the transverse planes with ACS were significantly higher than those sequences with PI (ACS (1.96 ± 1.38) vs. PI (1.59 ± 1.11), $p < 0.0003$). The CNR values of post-contrast

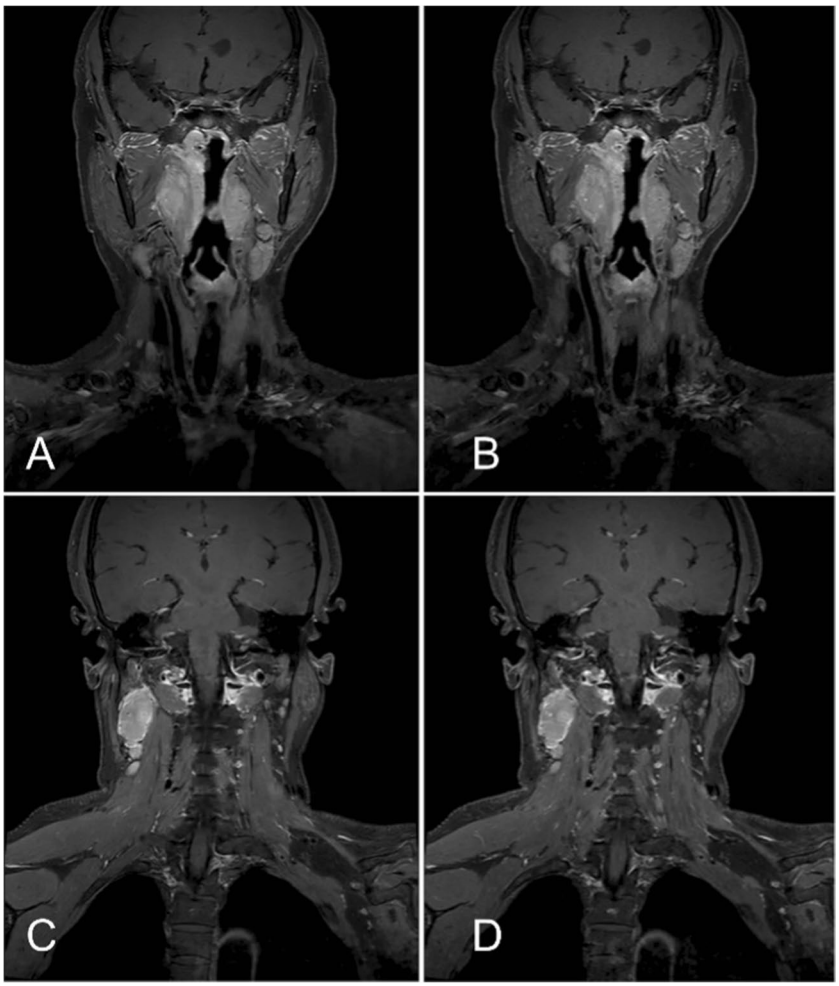

Fig. 3 A 54-year-old female patient with NPC. The MRI sequences and examination time were summarized as follows: post-contrast T1-weighted FSE sequences in the coronal planes: (**A**) and (**C**) with ACS technique (124 s); (**B**) and (**D**) with PI technique (216 s); ACS provided a better image quality than the PI, while the scan time was reduced over 40%

T1-weighted sequences in the transverse planes with ACS were significantly higher than those sequences with PI (ACS (4.59 ± 2.19) vs. PI (3.93 ± 2.03), $p < 0.0001$). The CNR values of post-contrast T1-weighted sequences in the coronal planes with ACS were significantly higher than those sequences with PI (ACS (9.32 ± 4.07) vs. PI (6.70 ± 2.54), $p < 0.0001$).

Table 4 shows that the scores of lesion detection, margin sharpness of lesions, artifacts, and overall image quality are higher in the ACS sequences than those in the PI sequences (p (for all) < 0.0001). The inter-observer agreement for the independent qualitative analysis showed satisfactory-to-excellent agreement, and κ value ranged from 0.627 to 0.892 (p (for all) < 0.0001).

Discussion

The present study explored whether applying ACS would decrease the examination time and affect the MR image quality of NPC by comparing with the PI.

The quantitative assessment in the study showed that with applying both the ACS and conventional PI for two sets of FSE sequences on the same patient, the sequence scanning time using ACS was significantly shorter than that by PI at the same resolution. The time of 4 sequences with ACS was 180 s shorter than that with the conventional PI, indicating that time saving was approximately equal to 35%. Meanwhile, the SNR and CNR values of images did not descend drastically, and these values were even higher in the sequences that used ACS, which indicated that ACS has the ability to maintain image quality even at high acceleration factors. In previous combined nasopharyngeal neck scans, the SI of the lower neck was mainly poor due to the limitation of the head and neck coil and the vascular pulsation artifacts after contrast injection, especially the fat suppression sequences in the coronal plane. Hence, the SNR of the coronal fat suppression sequence was deliberately measured. It was found that the SNR of the trapezius muscle with ACS was higher than with the conventional PI, while the scan time was reduced over 40%, indicating that ACS could also maintain the imaging quality after the imaging velocity was

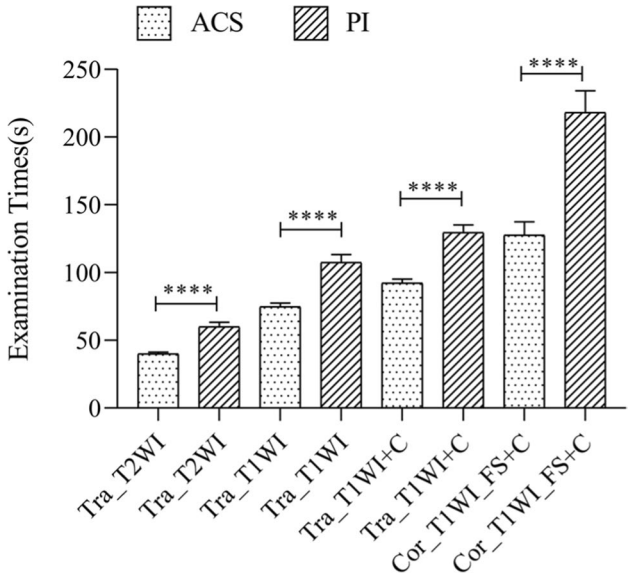

Fig. 4 Comparison of examination time between ACS sequences and PI sequences

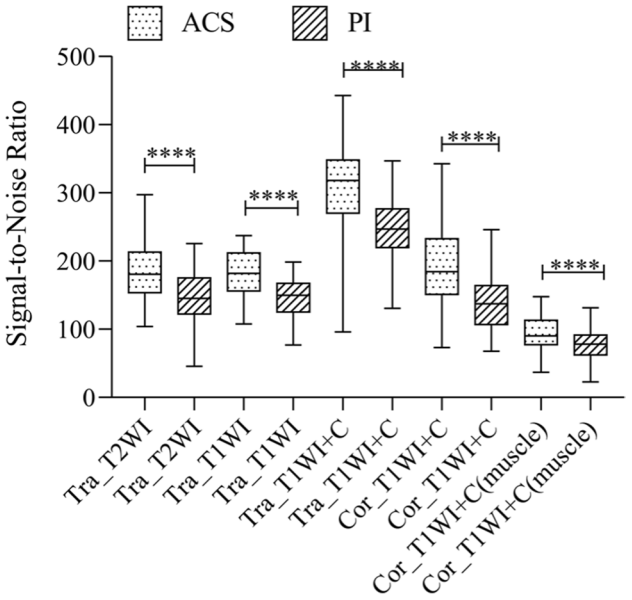

Fig. 5 Comparison of SNR values between ACS sequences and PI sequences. ACS sequences were significantly higher than FSE sequences with PI technique

raised. ACS can make a well-balanced relationship between the imaging velocity and imaging quality.

The qualitative assessment in the study showed that the scores of the sequences with ACS were higher than with PI in lesion detection, margin sharpness of lesions, artifacts, and overall image quality. Inter-observer agreement was evaluated for all qualitative indicators for each method, and the results showed that the values of kappa ranged from 0.627 to 0.892. Therefore, satisfactory-to-excellent agreement was achieved in the present study. We found that margin sharpness of NPC lesions was clearer for FSE sequences with ACS, and the ACS-based sequences could clearly distinguish muscles, mucosa membranes, and adipose tissues compared with the PI-based sequences. It could be advantageous to more clearly define the invasion range of the tumor tissues, especially for T2-weighted FSE sequences in the transverse planes. This characteristic may be related to the ability of ACS to suppress noises and reduce artifacts, resulting in a higher image clarity and a better overall quality than those achieved by the PI method. The PI might produce residual aliasing and noise-induced artifacts at high acceleration factors, which were previously reported [11, 33–36]. However, ACS has eliminated this challenge perfectly. The AI module in ACS was trained using a huge amount of fully sampled data to suppress various reconstruction artifacts introduced by conventional methods at high acceleration factors without affecting anatomical and pathological structures. Patients with NPC may easily produce swallowing motion artifacts in MR scans, and in severe cases, they may not be able to complete the entire examination. However, the motion

Table 3 Quantitative comparison of SNR and CNR values between the two methods

	Method	ACS (mean ± SD)	PI (mean ± SD)	*p* value
SNR	Tra_T2WI_FSE	182.07 ± 41.69	145.27 ± 38.05	< 0.0001
	Tra_T1WI_FSE	183.53 ± 31.36	147.02 ± 27.11	< 0.0001
	Post contrast Tra_T1WI_FSE	312.43 ± 56.59	245.89 ± 46.68	< 0.0001
	Post contrast Cor_T1WI_FSE	189.05 ± 60.84	140.82 ± 43.26	< 0.0001
	Post contrast Cor_T1WI_FSE (muscle)	94.76 ± 27.08	78.63 ± 23.00	< 0.0001
CNR	Tra_T2WI_FSE	6.21 ± 3.00	5.52 ± 3.05	< 0.0027
	Tra_T1WI_FSE	1.96 ± 1.38	1.59 ± 1.11	< 0.0003
	Post contrast Tra_T1WI_FSE	4.59 ± 2.19	3.93 ± 2.03	< 0.0001
	Post contrast Cor_T1WI_FSE	9.32 ± 4.07	6.70 ± 2.54	< 0.0001

SNR, signal-to-noise ratio; *CNR*, contrast-to-noise ratio

p values were calculated using the paired sample *t*-test

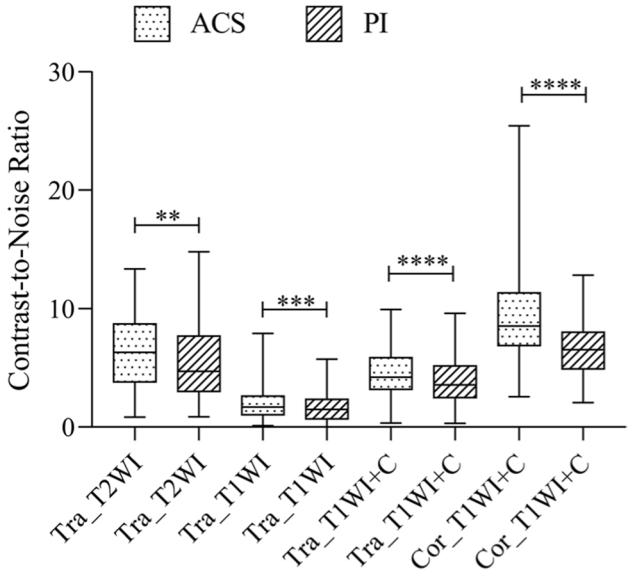

Fig. 6 Comparison of CNR values between ACS sequences and PI sequences

artifacts caused by swallowing motions were significantly reduced in the sequences using ACS in the present study. The ultra-fast imaging of ACS, which is the inherent ability of freeze motions to effectively reduce the artifacts, could be an influential factor.

Unlike the PI method, there are potential risks existing when using ACS from the deep learning method, whose high precision heavily depends on the size and variety of the training data set. Although the current deep learning algorithms have already shown accurate reconstruction results, the results still lack stability. The issues of instability majorly cover the following aspects: (1) the instability of some small noise perturbations; (2) the instability of microstructure changes; (3) the instability of sample number difference. In medical imaging, stability and accurate image reconstruction methods are essential for disease diagnosis. Thus, it is very significant to ensure stable outputs while improving the accuracy of the algorithm. However, according to the current research, the capability of ACS in lesion detection is no less than that of PI. Taking the T2WI FSE sequence as the example, 0 cases were rated 1 and 2 (1, poor, almost invisible; 2, fair, lesions were partially visible) by both readers on the ACS and PI methods.

At present, deep learning–based MRI solutions are used to solve problems, such as artifact reduction, motion correction, and denoising, which are mainly divided into two categories: deep learning–based image reconstruction and deep learning–based image post-processing [37, 38]. The method of deep learning–based image post-processing uses deep learning reconstruction tools integrated into MRI, separating MRI signals from noises by deep learning algorithms, to enhance the signal intensity, while suppressing noises [18, 39]. The ACS is the method belonging to deep learning–based image reconstruction, integrating AI module into the iterative reconstruction process of the compression perception framework, and some researchers demonstrated that this deep learning method helps the reconstruction of CS and ensures high fidelity when acquisition duration prolongs [40–42].

There are still several shortcomings in the present study. Firstly, the small sample size might cause a selection bias in the measured values. Secondly, only NPC patients with definite pathological results and typical imaging manifestations were included, while patients with other nasopharyngeal lesions were excluded. Last but not least, although the ACS has the feature of noise reduction to decrease the artifacts, some inherent artifacts might still not be eliminated.

Table 4 Comparison of subjective evaluation scores and inter-observer kappa values between ACS sequences and PI sequences

Method	Lesion detection		Margin sharpness of lesions		Artifacts		Overall image quality	
	Subjective evaluation	Kappa	Subjective evaluation	Kappa	Subjective evaluation	Kappa	Subjective evaluation	Kappa
Tra_T2WI_ACS	4.89 ± 0.31	0.841	4.92 ± 0.27	0.784	4.88 ± 0.33	0.858	4.91 ± 0.29	0.817
Tra_T2WI_PI	3.86 ± 0.46	0.691	3.73 ± 0.45	0.773	4.11 ± 0.40	0.794	3.92 ± 0.38	0.780
Tra_T1WI_ACS	4.00 ± 0.21	0.660	4.08 ± 0.33	0.640	4.45 ± 0.56	0.892	4.02 ± 0.21	0.660
Tra_T1WI_PI	3.38 ± 0.49	0.627	3.11 ± 0.32	0.776	3.80 ± 0.42	0.719	3.36 ± 0.48	0.664
Tra_T1WI + C_ACS	4.85 ± 0.36	0.882	4.61 ± 0.53	0.851	3.95 ± 0.27	0.790	4.59 ± 0.52	0.822
Tra_T1WI + C_PI	3.93 ± 0.33	0.784	3.68 ± 0.48	0.867	3.30 ± 0.58	0.866	3.79 ± 0.43	0.831
Cor_T1WI + C_ACS	4.84 ± 0.41	0.727	4.84 ± 0.41	0.836	4.04 ± 0.26	0.884	4.83 ± 0.42	0.847
Cor_T1WI + C_PI	3.96 ± 0.31	0.756	3.84 ± 0.37	0.830	3.40 ± 0.58	0.868	3.88 ± 0.37	0.886

p values were calculated using the Wilcoxon signed rank test. All values were presented as mean ± standard deviation of the scores (*p* (for all) < 0.0001). Inter-observer agreement for image analyses was assessed by the weighted kappa values (*p* all < 0.0001)

In conclusion, compared with the PI technique, the ACS technique for MR examination of NPC can not only reduce scanning time, but also improve image quality.

Acknowledgements We would like to express our thanks to Liyun Zheng from United Imaging Healthcare for her help in manuscript revision and we thank Shuheng Zhang for providing technical comments.

Funding The authors state that this work has not received any funding.

Declarations

Guarantor The scientific guarantor of this publication is Guixiao Xu (corresponding author).

Conflict of interest The authors declare that there is no conflict of interest.

Statistics and biometry No complex statistical methods were necessary for this paper.

Informed consent Written informed consent was obtained from all patients in this study.

Ethical approval Institutional review board approval was obtained.

Methodology
- retrospective
- observational study
- performed at one institution

References

1. Chen YP, Chan ATC, Le QT, Blanchard P, Sun Y, Ma J (2019) Nasopharyngeal carcinoma. Lancet 394:64–80
2. Liao XB, Mao YP, Liu LZ et al (2008) How does magnetic resonance imaging influence staging according to AJCC staging system for nasopharyngeal carcinoma compared with computed tomography? Int J Radiat Oncol Biol Phys 72:1368–2137
3. Tang LL, Chen YP, Chen CB et al (2021) The Chinese Society of Clinical Oncology (CSCO) clinical guidelines for the diagnosis and treatment of nasopharyngeal carcinoma. Cancer Commun (Lond) 41:1195–1227
4. Razak AR, Siu LL, Liu FF, Ito E, O'Sullivan B, Chan K (2010) Nasopharyngeal carcinoma: the next challenges. Eur J Cancer 46:1967–1978
5. Lv J, Wang C, Yang G (2021) PIC-GAN: a parallel imaging coupled generative adversarial network for accelerated multi-channel MRI reconstruction. Diagnostics (Basel) 11:61
6. Li Y, Dumoulin C (2012) Correlation imaging for multiscan MRI with parallel data acquisition. Magn Reson Med 68:2005–2017
7. Li Y, Edalati M, Du X, Wang H, Cao JJ (2018) Self-calibrated correlation imaging with k-space variant correlation functions. Magn Reson Med 79:1483–1494
8. Noll DC, Nishimura DG, Macovski A (1991) Homodyne detection in magnetic resonance imaging. IEEE Trans Med Imaging 10:154–163
9. Huang F, Lin W, Li Y (2009) Partial fourier reconstruction through data fitting and convolution in k-space. Magn Reson Med 62:1261–1269
10. Lustig M, Pauly JM (2010) SPIRiT: iterative self-consistent parallel imaging reconstruction from arbitrary k-space. Magn Reson Med 64:457–471
11. Deshmane A, Gulani V, Griswold MA, Seiberlich N (2012) Parallel MR imaging. J Magn Reson Imaging 36:55–72
12. Tam LK, Galiana G, Stockmann JP, Tagare H, Peters DC, Constable RT (2015) Pseudo-random center placement O-space imaging for improved incoherence compressed sensing parallel MRI. Magn Reson Med 73:2212–2224
13. Feng L, Benkert T, Block KT, Sodickson DK, Otazo R, Chandarana H (2017) Compressed sensing for body MRI. J Magn Reson Imaging 45:966–987
14. Lustig M, Donoho D, Pauly JM (2007) Sparse MRI: the application of compressed sensing for rapid MR imaging. Magn Reson Med 58:1182–1195
15. Yokota Y, Takeda C, Kidoh M et al (2021) Effects of deep learning reconstruction technique in high-resolution non-contrast magnetic resonance coronary angiography at a 3-Tesla machine. Can Assoc Radiol J 72:120–127
16. Qiu D, Zhang S, Liu Y, Zhu J, Zheng L (2020) Super-resolution reconstruction of knee magnetic resonance imaging based on deep learning. Comput Methods Programs Biomed 187:105059
17. Hammernik K, Klatzer T, Kobler E et al (2018) Learning a variational network for reconstruction of accelerated MRI data. Magn Reson Med 79:3055–3071
18. Ueda T, Ohno Y, Yamamoto K et al (2021) Compressed sensing and deep learning reconstruction for women's pelvic MRI denoising: utility for improving image quality and examination time in routine clinical practice. Eur J Radiol 134:109430
19. Wang S, Cao G, Wang Y et al (2021) Review and prospect: artificial intelligence in advanced medical imaging. Frontiers in Radiology 1:781868
20. Yang X, Wu Q, Wu F, Zhong Y (2021) Differential expression of COL4A3 and collagen in upward and downward progressing types of nasopharyngeal carcinoma. Oncol Lett 21:223
21. Yao JJ, Zhou GQ, Zhang F et al (2016) Neoadjuvant and concurrent chemotherapy have varied impacts on the prognosis of patients with the ascending and descending types of nasopharyngeal carcinoma treated with intensity-modulated radiotherapy. PLoS One 11:e0161878
22. Ng WT, Yuen KT, Au KH, Chan OS, Lee AW (2014) Staging of nasopharyngeal carcinoma–the past, the present and the future. Oral Oncol 50:549–554
23. Yu E, O'Sullivan B, Kim J, Siu L, Bartlett E (2010) Magnetic resonance imaging of nasopharyngeal carcinoma. Expert Rev Anticancer Ther 10:365–375
24. Zhang LL, Huang MY, Li Y et al (2019) Pretreatment MRI radiomics analysis allows for reliable prediction of local recurrence in non-metastatic T4 nasopharyngeal carcinoma. EBioMedicine 42:270–280
25. Zhou X, He X, Xue F, Ou X, Hu C (2020) Impact of paranasal sinus invasion on oncologic and dosimetric outcomes in nasopharyngeal carcinoma following intensity-modulated radiation therapy-implications for risk stratification and planning optimization. Front Oncol 10:407

26. Dutoit JC, Verstraete KL (2016) MRI in multiple myeloma: a pictorial review of diagnostic and post-treatment findings. Insights Imaging 7:553–569
27. Silva JR Jr, Hayashi D, Yonenaga T et al (2013) MRI of bone marrow abnormalities in hematological malignancies. Diagn Interv Radiol 19:393–399
28. Gu J, Wang Z, Kuen J et al (2018) Recent advances in convolutional neural networks. Pattern Recogn 77:354–377
29. Ledig C, Theis L, Huszár F et al (2017) Photo-realistic single image super-resolution using a generative adversarial network. 2017 IEEE Conference on Computer Vision and Pattern Recognition (CVPR), pp 105–114
30. Isola P, Zhu J, Zhou T, Efros AA (2017) Image-to-image translation with conditional adversarial networks. 2017 IEEE Conference on Computer Vision and Pattern Recognition (CVPR), pp 5967–5976
31. Sheng RF, Zheng LY, Jin KP et al (2021) Single-breath-hold T2WI liver MRI with deep learning-based reconstruction: a clinical feasibility study in comparison to conventional multi-breath-hold T2WI liver MRI. Magn Reson Imaging 81:75–81
32. National Electrical Manufacturers Association (2008) NEMA MS 1-2008 determination of signal-to-noise ratio (SNR) in diagnostic magnetic resonance imaging. national electrical manufacturers association, Arlington. Available via https://webstore.ansi.org/standards/nema/nemams2008. Accessed 1 Jan 2008
33. Bustin A, Lima da Cruz G, Jaubert O, Lopez K, Botnar RM, Prieto C (2019) High-dimensionality undersampled patch-based reconstruction (HD-PROST) for accelerated multi-contrast MRI. Magn Reson Med 81:3705–3719
34. Hamilton J, Franson D, Seiberlich N (2017) Recent advances in parallel imaging for MRI. Prog Nucl Magn Reson Spectrosc 101:71–95
35. Hoge WS, Brooks DH (2008) Using GRAPPA to improve autocalibrated coil sensitivity estimation for the SENSE family of parallel imaging reconstruction algorithms. Magn Reson Med 60:462–467
36. Lv J, Wang P, Tong X, Wang C (2020) Parallel imaging with a combination of sensitivity encoding and generative adversarial networks. Quant Imaging Med Surg 10:2260–2273
37. Lin DJ, Johnson PM, Knoll F, Lui YW (2021) Artificial intelligence for MR image reconstruction: an overview for clinicians. J Magn Reson Imaging 53:1015–1028
38. Chandra SS, Bran Lorenzana M, Liu X, Liu S, Bollmann S, Crozier S (2021) Deep learning in magnetic resonance image reconstruction. J Med Imaging Radiat Oncol 65:564–577
39. Naganawa S, Nakamichi R, Ichikawa K et al (2021) MR imaging of endolymphatic hydrops: utility of iHYDROPS-Mi2 combined with deep learning reconstruction denoising. Magn Reson Med Sci 20:272–279
40. Yang G, Yu S, Dong H et al (2018) DAGAN: deep de-aliasing generative adversarial networks for fast compressed sensing MRI reconstruction. IEEE Trans Med Imaging 37:1310–1321
41. Sun L, Fan Z, Fu X, Huang Y, Ding X, Paisley J (2019) A deep information sharing network for multi-contrast compressed sensing MRI reconstruction. IEEE Trans Image Process 28:6141–6153
42. Ouchi S, Ito S (2021) Reconstruction of compressed-sensing MR imaging using deep residual learning in the image domain. Magn Reson Med Sci 20:190–203